Composites Part B 193 (2020) 108018

Contents lists available at ScienceDirect

Composites Part B

journal homepage: www.elsevier.com/locate/compositesb

Modelling and parameter optimization for filament deformation in 3D cementitious material printing using support vector machine

Zhixin Liu, Mingyang Li, Yiwei Weng, Ye Qian, Teck Neng Wong *, Ming Jen Tan

Singapore Centre for 3D Printing, School of Mechanical & Aerospace Engineering, Nanyang Technological University, 50 Nanyang Avenue, 639798, Singapore

ARTICLE INFO

Keywords:
3D cementitious material printing
Numerical model
Flow mechanism
Filament deformation
Combine effects study
Support vector machine

ABSTRACT

The material flow mechanism affects the printing quality considerably in 3D cementitious material printing (3DCMP) area. A numerical model was developed to investigate the material flow mechanism during the extrusion and deposition process. To quantify the effects of flow mechanism on the filament printing quality, deformation of the printed filament was proposed. Then a Support Vector Machine (SVM) was employed to study various factors on flow mechanism, hence the deformation of the printed filament. The SVM model results showed that deformation of the printed filament is independent of plastic viscosity, however, material yield stress and relative nozzle travel speed significantly affect the deformation of the printed filament. Lastly, an empirical parametric associative model was proposed to predict the filament deformation based on material yield stress and relative nozzle travel speed.

1. Introduction

Additive manufacturing (AM), also known as 3D printing, has attracted much attention from academic sectors and industries recently due to its advantages: labour saving, less waste and high freedom of designing as reported by Chua et al. [1]. According to Paul et al. [2], 3D cementitious material printing (3DCMP) builds structure without any formwork or mold making and is gaining ground in the construction area.

Numerous investigations have been conducted from various perspectives, such as materials, printing process and printing system on 3DCMP [3–13]. Now 3DCMP has pass its infancy stage, surface finish of the filament becomes more and more important, hence, Bastani et al. [14] did some investigations on it and reported that surface finishing of the printed filament depends on the flow pattern of the cementitious material significantly, which is determined by the geometry of the nozzle, material rheological properties and the process parameters of the printing system. To investigate the effects of nozzle shape on the deformation of the printed filament, various shape nozzles have been investigated experimentally. Kwon et al.'s experimental results showed that the surface finishing of the filament printed using rectangular nozzle is much better than that using the round nozzle or elliptic nozzle [15]. Recently, Lao et al. [16] reported that slightly changing the shape of rectangular nozzle can improve surface finishing significantly. Then the image processing method has been adopted by Panda et al. to analysis the deformation of the concrete filament during the printing process qualitatively, the flow mechanism of the material was ignored [17]. The impacts of process parameters on the cross-section of the printed polymer filament have been investigated experimentally as well [18]. The review showed that the effects of material rheological properties, such as: dynamic yield stress and plastic viscosity, on the deformation of the printed filament was not investigated. These investigations aimed at optimizing the process parameters from experimental data during the printing process. However, to optimize the materials properties and process parameters during the printing process, a thorough understanding especially numerical study of the flow behaviour of non-Newtonian cementitious material is critical. Although, the extrusion based 3D printing is difficult to simulate due to the multi phases flow existing in various spatial and temporal scales as reported by Comminal [19], various numerical 2D and 3D models have been proposed to study the temperature and stress distribution the polymeric material and good results have been obtained [20–23]. Mcllroy et al. studied the deformation of the polymer chains after deposition using the round nozzle numerically as well [24,25]. Most of investigations have been conducted on temperature, stress distribution and cross-section of the printed polymeric material. Asprone et al. studied the failure mechanisms and stress distribution of the 3DCMP printed filaments numerically [6], and Kwon [26] investigated the influence of the nozzle

* Corresponding author.
E-mail address: MTNWONG@ntu.edu.sg (T.N. Wong).

https://doi.org/10.1016/j.compositesb.2020.108018
Received 19 June 2019; Received in revised form 27 March 2020; Accepted 28 March 2020
Available online 31 March 2020

shape on the cementitious material flow behaviour numerically. However, few numerical studies have been conducted on cementitious material printing process and the dynamic behaviour on deformation of the printed cementitious material filament. The impacts of the material rheological properties and process parameters on the printing quality were not characterized quantitatively as well. Hence, a thorough understanding of the flow behaviour of non-Newtonian cementitious material is critical in improving the printing quality of the filament and a parameter should be proposed to characterize the printing quality. In this study, a numerical simulation was undertaken to understand the flow mechanism and one paramater Φ_F ($\Phi_F = L_b/L_t$), which refers to the ratio of the bottom length to the top length of the cross-section of the printed filament, was proposed to characterize the printing quality in this study.

Bos et al. [27] revealed that optimal selections of the rheological properties of the cementitious material and the process parameters of the printing system are crucial to decrease the deformation of the filament and improve the surface finishing of the products. The combined impact of material rheological properties and process parameters on printing quality was shown to be important in the Al alloy [28] and cementitious material extrusion process [29,30]. However, the combined effect of the rheological properties and process parameters was not studied. Hence, in this paper, the combined effect on the flow mechanism is studied. More than 200 cases were studied numerically to understand the flow mechanism at various conditions. Then the machine learning technique, Support Vector Machine (SVM), was adopted to study the combined effects of rheological properties and process parameters on the deformation of the printed filament.

2. Theories

2.1. Numerical approach

In order to track the interface between the cementitious material and air, the volume of fluid (VOF) is adopted to simulate the cementitious material flow and deposition.

The governing equations of the VOF formulations on multiphase flow are shown as follows:

Continuity equation

$$\frac{\partial \rho}{\partial t} + \nabla \cdot (\rho \vec{v}) = 0 \tag{1}$$

Equation of motion

$$\frac{\partial (\rho \vec{v})}{\partial t} + \nabla \cdot (\rho \vec{v} \vec{v}) = -\nabla p + \nabla \cdot \tau + \rho g \tag{2}$$

Volume fraction equation

$$\frac{\partial \alpha_m}{\partial t} + \vec{v} \cdot \nabla \alpha_m = 0 \tag{3}$$

$$\tau = \tau_0 + k\dot{\gamma} \tag{4}$$

where $\rho = \alpha_c \rho_c + \alpha_a \rho_a$, $k = \alpha_c k_c + \alpha_a$. α_m is the volume fraction of m-th fluid in the system. $\dot{\gamma}$ (s^{-1}) is shear rate. τ_0 (Pa) is the yield stress. ρ_c (kg/m^3) and ρ_a (kg/m^3) are the density of the cementitious material and air, respectively. k_c (Pa·s) is the plastic viscosity of cementitious material and k_a (Pa·s) is the viscosity of air.

2.2. Support vector machine (SVM) for feature classification

Various methods were proposed to characterize the combined effects of factors on the response. According to Abdul el al. [12,31,32], the statistical design of experiments (DoE) is able to capture the interaction effect, however, Chen et al. [33] mentioned that the interaction effect can be captured only when weak nonlinear relation between variables and response could be assumed. Although Artificial Neural Network (ANN) could be used to characterize the interaction effects, it suffers from the problem of overfitting as reported by Yao et al. [34]. Kothuru et al. [35] concluded that these methods have the limitation of requiring complex data for better correlation of the factors and responses. Machine learning has been successfully used in manufacturing by Cho et al. [36] and grinding area by Chiu et al. [37] recently due to its advantages: better generalization ability, less data and better scalability as reported by Rao et al. [38]. However, the application of machine learning in 3D cementitious material printing is less explored. Hsueh et al. [39] demonstrated that the machine learning technique, such as support vector machine (SVM), can overcome the issues existing in conventional statistical methods and it can be interpreted easily from the perspective of geometry. **S**VM classifies the data into two categories by constructing a decision function based on mathematical theory. A hyperplane with maximum margin between the two categories for best classification will be determined by a set of data points (support vector). Below is a short discussion about SVM.

For a set of input data (x_i, y_i, i = 1,2,3 … n), SVM is to separate them into two parts with high accuracy by transferring the current plane into a high dimensional space through non-linear mapping. The separation plane within the high dimensional space is constructed by: $\vec{w} \cdot \vec{x_i} + b = 0$, where $\vec{w}$ is the normal vector of the plane and b is the intercept as reported by Zhou et al. [40]. For all the testing sample data $\vec{x_i}$,

$$\begin{cases} \vec{w} \cdot \vec{x_i} + b \geq 1 & if\ y_i = 1 \\ \vec{w} \cdot \vec{x_i} + b \leq -1 & if\ y_i = -1 \end{cases} \tag{5}$$

The distance from x_i to the plane is $\frac{\|\vec{w} \cdot \vec{x_i} + b\|}{\|\vec{w}\|}$ and the nearest distance from the testing data to the plane is $\frac{1}{\|\vec{w}\|}$. The target is to determine the largest $\frac{1}{\|\vec{w}\|}$ subject to the constraints $\vec{w} \cdot \vec{x_i} + b = 0$. It is convenient to minimize the $\frac{\|\vec{w}\|^2}{2}$. It can be solved by adopting Lagrange function as follows:

$$L_{(w,b,\lambda)} = \frac{\|\vec{w}\|^2}{2} - \sum_i^n \lambda_i (y_i (\vec{w} \cdot \vec{x_i} + b) - 1) \tag{6}$$

The partial derivatives of the function with respect to w and b is set to be zero

$$\frac{\partial L_{(w,b,\lambda)}}{\partial w} = 0 \quad \text{and} \quad \frac{\partial L_{(w,b,\lambda)}}{\partial b} = 0 \tag{7}$$

Then $w^T = \sum_1^n \lambda y_i \vec{x_i}$, $\sum_1^n \lambda_i y_i = 0$, $0 \leq \lambda_i \leq C$. Substituting them into the objective function

$$f = \sum_i^n \lambda_i - \frac{1}{2} \sum_{i,j}^n \lambda_i \lambda_j y_i y_j \vec{x} \cdot \vec{x_j} \tag{8}$$

Subject to $\sum_1^n \lambda_i y_i = 0$. After solving it, a set of λ_j and $b_j$were obtained. A decision function is then determined from the training samples

$$f = \sum_j^n \lambda_j y_j \vec{x} \cdot \vec{x_j} + b_j \tag{9}$$

If the data cannot be classified linearly, the kernel function $k(\vec{x}, \vec{x_j})$ should be adopted to modify the decision function as

$$f = \sum_j^n \lambda_j y_j k(\vec{x}, \vec{x_j}) + b_j \tag{10}$$

In this study, the Gaussian kernel function $k(\vec{x} \cdot \vec{x_j}) = e^{(-\gamma(\vec{x} - \vec{x_j})^T (\vec{x} - \vec{x_j}))}$ was applied to construct the decision model and classify the patterns.

3. Numerical simulation scheme and experiments validation

3.1. Simulation scheme

The commercial CFD (Computational Fluid Dynamics) package ANSYS FLUENT was used to perform the numerical simulation. The model geometry was meshed with the preprocessor ICEM software and imported to the FLUENT for calculation. Fig. 1 shows the geometry of material extrusion and deposition of 3DCMP in numerical simulation. It comprises of a vertical inlet zone and a horizontal deposit zone. A stream of cementitious material is fed into the inlet zone which then flows into the deposit zone. The cross-section of the inlet zone is 30 mm × 15 mm (L × W) while the cross-section of the deposit zone is 45 mm × 15 mm (W × H). The height of the inlet zone is 30 mm. The length of the deposit zone is 125 mm.

A segregated time dependent solver was used in the simulation. The boundary conditions are: the velocity inlet for the cementitious material is specified as uniform. The outlet is atmosphere pressure. The PRESTO was selected for the pressure interpolation and the PISO was selected for pressure-velocity coupling. A second-order up-wind differentiating scheme is used for differentiating the momentum equation. The implicit body force treatment was implemented for body force formulation. In addition, the time scale was set as $\Delta t = 5 \times 10^{-4}$ s and relaxation factor was adjusted to ensure the convergence. The system is maintained at room temperature and atmosphere pressure at the outlet. The assumptions are as follows:

1. The material flows uniformly into the nozzle;
2. As the material extrusion and deposition process only take 2 s, cement hydration effect and thixotropy behaviour can be ignored during the simulation;
3. There is no slip at the interface of the nozzle;
4. As the material viscosity is large and the material velocity is small, the Reynold number is less than 1.0. Therefore, the flow in the inlet zone is steady, laminar flow without any secondary flow or turbulent flow in it;

3.2. Simulation results

Fig. 2 shows the typical result of the extrusion process within the nozzle. It is clear that the cementitious material was retarded and sheared near the wall [41]. The flow rate at the centre of the nozzle is higher than that near the inner surface of the nozzle, which may lead to the warp at the edge of the bottom wall of the printed filament.

Fig. 3 shows the deposition process of the material, through which a quantitative understanding of the deposition process can be obtained. At

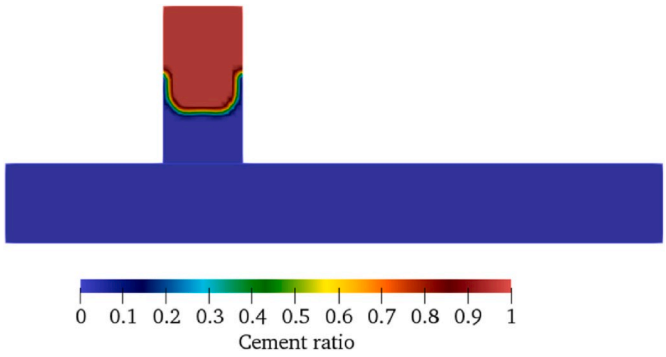

Fig. 2. The profile of the cementitious material within the nozzle.

the initial time, the inlet zone and the deposition zone were filled with air. At time zero, the cementitious material flowed into the nozzle with a constant velocity. The nozzle started to move (50 mm/s to 70 mm/s) when the extruded material approximately touched the bottom wall. After the nozzle travelled for 0.3 s, the flow became fully developed within the deposition zone, which shows that the initial deposit process has no effect on the deformation of the printed material. The numerical simulation stopped when the total flow time is approximately 2 s. To characterize the deformation of the printed filament, one parameter Φ_F (deformation ratio $\Phi_F = L_b/L_t$), which refers to the ratio of the bottom length to the top length of the cross-section of the printed filament, is proposed. The cross-section refers to the plane where the material deposited for almost 1 s, as shown in Fig. 3. This plane was selected to remove the effect of deposition time on the deformation of the printed filament.

3.3. Experimental validation of the numerical model

The equipment used in 3DCMP was a 4-axis gantry printer (see Fig. 4). During the printing process, cement, sand, fly ash, and silica fume were mixed homogeneously in the mixer and pumped through a hose with 3 m in length and 25.4 mm in diameter. The well mixed material was extruded from a rectangular nozzle with a 30 mm × 15 mm (L × W) dimension. The standoff distance between the nozzle tip and the printing bed was set to be 15 mm as well. Before the printing experiments, the pumping flow rate was calibrated by controlling the width of printed filament at approximately 30 mm (±1 mm).

To validate the numerical method of simulating material extrusion and deposition process at different process parameters, some experiments were carried out. In the experiments, material one (M1) was

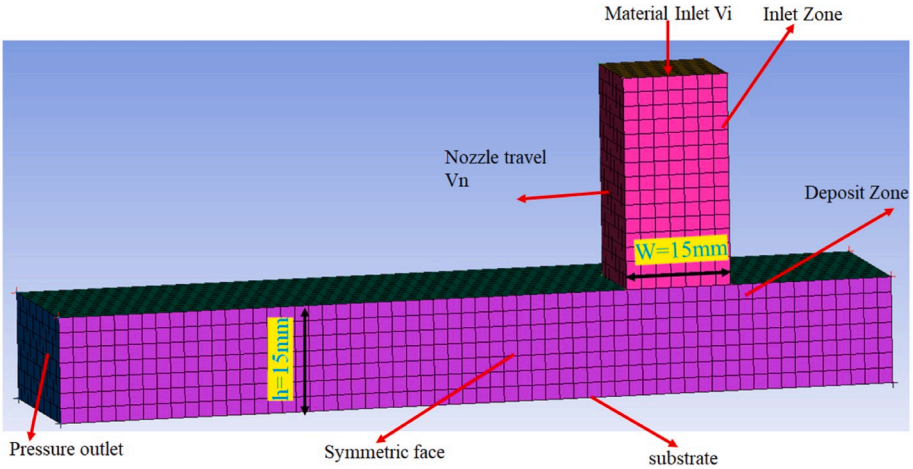

Fig. 1. Geometry of material extrusion and deposition of 3DCMP used in simulation.

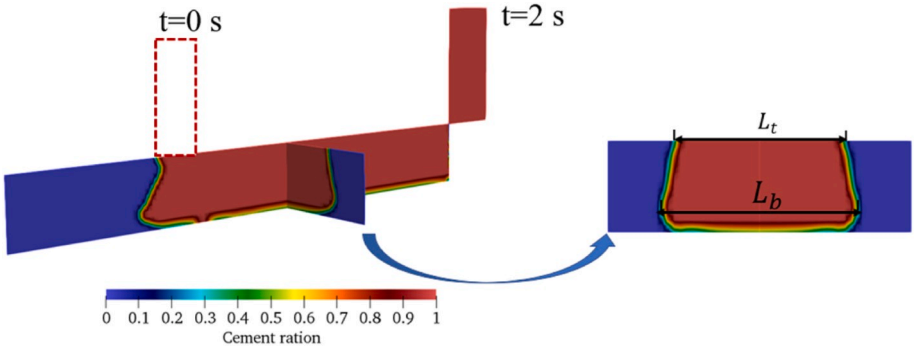

Fig. 3. Deposition of the printed filament at various time.

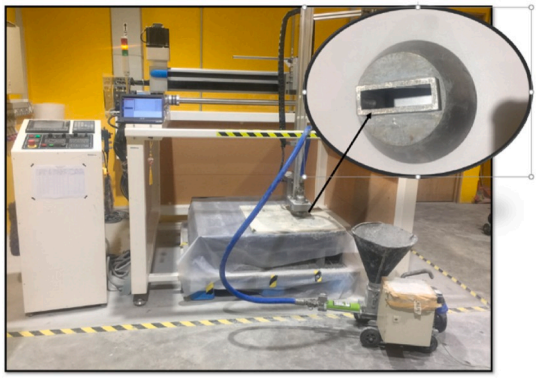

Fig. 4. The printing system used for 3DCMP.

adopted first. The rheological properties measurement results were shown in Fig. 5. Material rheological experiments were repeated for three times and the average value was regarded as the material rheological properties. The yield stress of the cementitious materials (M1) was 516 Pa and the plastic viscosity was 6.5 Pa·s. The density of the cementitious material was 2200 kg/m^3. In the numerical model, the length of the deposition zone should be long enough to eliminate the effect of deposition time (material flow time on the printing bed) on the deformation of the printed filament.

To measure the deformation of the printed cementitious material filament, 60 cm long straight filaments were printed to make the printing stable. Since the first layer is affected by the possibly uneven printing bed, the filament was printed for two layers and only the second layer was chosen to analyze the deformation. Similar to Lao et al. [16] the filaments were cut after finishing the printing for 48 h and three samples were chosen randomly. The width of the top and bottom line of the second layer of the filament was obtained by analyzing the image (see Fig. 6) via a Matlab code. To quantitatively characterize the accuracy of the simulation results, the deformation of the printed filament was measured. The profile of some printed filament and numerical results are shown in Fig. 7.

To validate the numerical model at different material rheological properties. Another two materials (M2: τ_0 = 168 Pa, k=*37* (Pa s). M3: τ_0 = 141 Pa, k=*26* (Pa s)) were adopted in this report. All the comparison results for M1, M2 and M3 are shown in Fig. 8. It is clear that the numerical results are consistent with experimental results. The discrepancy between the numerical and experimental results might be caused by the fluctuation of the pumping flow rate during the printing process and the slight change in rheological properties after pumping. The deformation of the printed filament increases with the decrease of the nozzle moving speed at given inlet velocity (60 mm/s in this study).

4. Results and discussion

4.1. The effect of cementitious material rheological properties on the deformation of the printed filament

As reported by Lachemi et al. [42], the rheological properties of the high flowable material affect the flow behaviour greatly. However, few reported the effect of stiff cementitious material rheological properties on the extrusion deposition process and the deformation of the printed filament. In this study, a uniform design method was adopted to set up more than 40 cases (Appendix A). It can produce the representative cases within the working range, which has been demonstrated by Zhang et al. [43]. These cases were obtained from the validated CFD model. After the deformations were computed, the SVM model was used to investigate the effect of individual rheological properties, process parameters and their combinations. The plastic viscosity and yield stress of the cementitious material were used as the input patterns of the SVM model, while the deformation of the printed filament was adopted as the output pattern. The predicted deformation of the printed filament from the training process was classified into five patterns as marked by

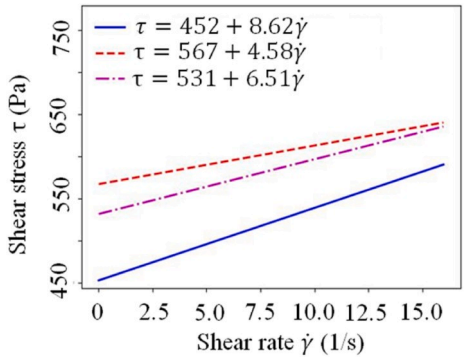

Fig. 5. Material rheological properties measurement results.

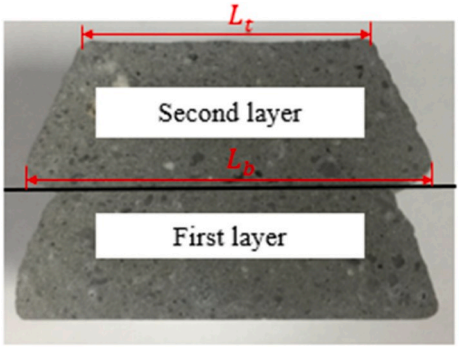

Fig. 6. Cross-section of the printed filament.

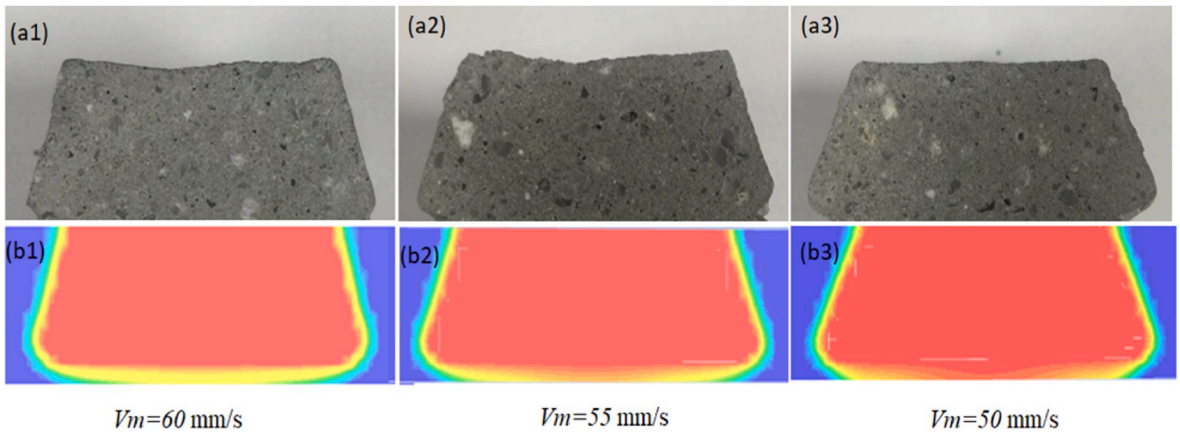

Fig. 7. Experimental and numerical simulation results of the cross-section of the printed filament at inlet velocity V_i = 0.06 m/s (a: experimental results; b: simulation results).

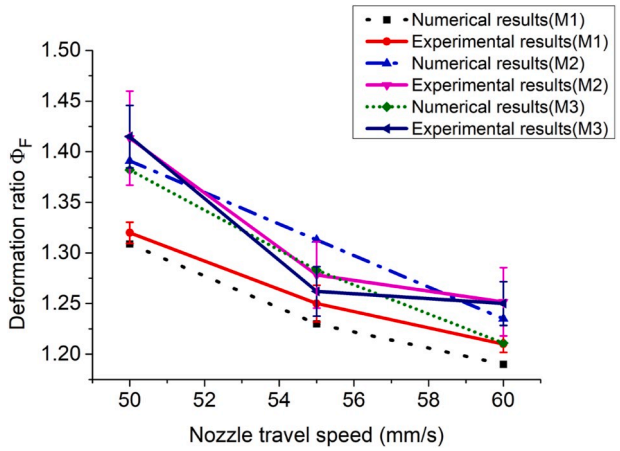

Fig. 8. Numerical prediction of the deformation of the printed filament with the experimental results.

various symbols. During the training process, about 50 sets of the data were implemented to train the SVM. Consequently, the decision function with maximum margin between the patterns was determined automatically and can be adopted to identify the pattern of the deformed filament according to the knowledge based on learning data. The SVM classification pattern from CFD simulated deformation of the printed filament is shown in Fig. 9. Most of the predicted points fall into the correct location for all the training data and the accuracy of the SVM model is higher than 0.9. It is clear from Fig. 9, the class line is approximately parallel to the x axis (refers to plastic viscosity), which means that material yield stress contributes to the deformation of the printed filament. In other words, the effect of the material plastic viscosity on the deformation of the printed filament can be ignored. The reasons for this phenomenon maybe threefold: firstly, the rheological properties of the cementitious material can be described by Bingham model and the shear viscosity of it can be written as

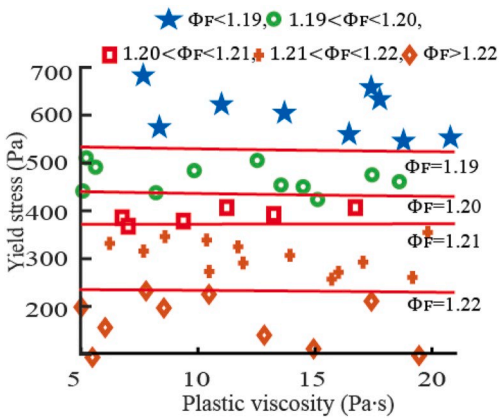

Fig. 9. SVM classification of the CFD simulated filament deformation vs material rheological properties.

$$\mu = \frac{\tau_0}{\dot{\gamma}} + k \tag{11}$$

Where μ (Pa·s) is shear viscosity, τ_0(Pa) is material dynamic yield stress, $\dot{\gamma}$ (s^{-1}) is shear rate and k (Pa·s) is plastic viscosity of the cementitious material. In this study, $\tau_0/\dot{\gamma}$ is much larger than the plastic viscosity (k), which means that the yield stress is dominant compared to plastic viscosity when controlling the shear viscosity. Secondly, as reported by Grandes et al. [44], water was filtrated to the surface of the cementitious material due to the irregular distribution of the pressure across the cross-section of the hose, which lead to a decrease of plastic viscosity (this term k decreases) at the inner surface of the hose during the delivery process. Therefore, the impact of the plastic viscosity on the shear viscosity decreased. Thirdly, as demonstrated by Wallevik [45], large particles tend to move away from the zone with large shear rate, which was near the inner surface of the hose in this study. In this case, due to particle migration, the material becomes heterogeneous. The friction resistance and interlocking between the particles increase yield stress (this term$\tau_0/\dot{\gamma}$increases) as reported by Liu et al. [46]. Hence, material yield stress is the main factor that affects the deformation of the printed filament.

The flow patterns and velocity distribution for different materials within half of the deposit zone are shown in Fig. 10. They were adopted to investigate the deformation of the printed filament qualitatively. The cement ratio mentioned in the study is describing the cementitious material to air ratio in the simulation. When the cement ratio is 1, it means the material exhibits 100% of the cementitious material behaviour. On the other hand, when the ratio is 0, it represents the atmospheric environment. The cementitious material to air ratio allows us to determine the interaction between the material and the environment and how the inter-region of the material behaves due to this interaction. Material flows perpendicularly to bottom part of the deposition zone. However, the magnitudes of the velocities are different. For various material yield stresses, the high velocity zone (velocity is higher than 0.02 m/s and marked out by the rectangle) is larger (see Fig. 10 (a)) compared that in Fig. 10 (b), which means that the lower material yield stress, the higher the velocity in the deposition zone. It indicates that the

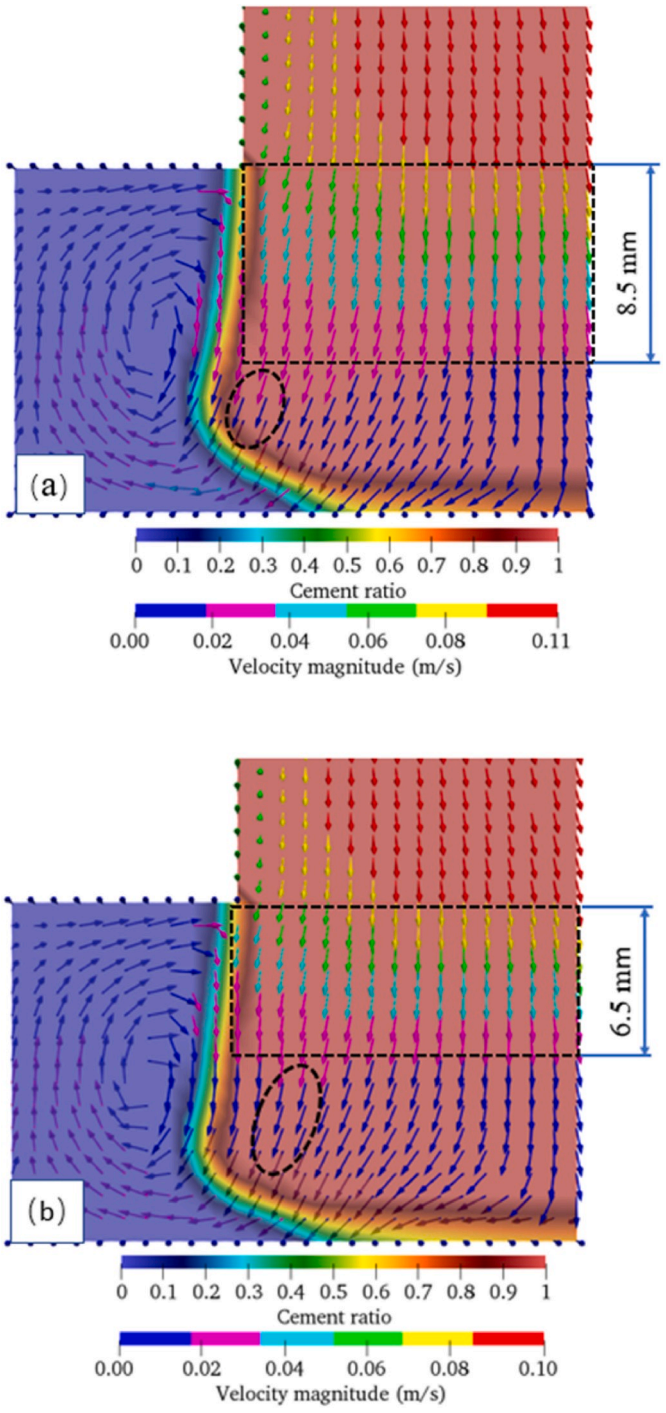

Fig. 10. The flow pattern and velocity distribution of materials with different dynamic yield stress τ_0 (a) $\tau_0 = 200$ Pa, (b) $\tau_0 = 516$ Pa.

pressure of the materials in this zone is high. According to Kwon et al. [26], if the pressure on the deposited zone goes beyond the optimal value, it will press the material to the lower pressure zone, which is the lower left corner in this study as shown in Fig. 10 (marked out by the circle), leading to the deformation of the printed filament.

4.2. The effects of process parameters on the deformation of the printed filament

As mentioned above, material yield stress dominates the deformation of the printed filament when the material inlet velocity is equal to the nozzle travel speed. However, investigations were rarely conducted to study the combined effects of rheological properties and process parameters on the deformation of the printed filament. Hence, in this part, the plastic viscosity, yield stress of the cementitious material and nozzle travel speed were used as the input variables of the SVM model to investigate the combined effect on the deformation of the printed filament. In practical printing, the deformation of the printed filament is expected to be smaller than $= 1.2$. Hence, 1.2 is selected as the criterion in this study. For the output pattern, the label of −1 refers to the deformation of the printed filament smaller than 1.2, on the other hand, the label of 1 corresponds to the deformation of the printed filament larger than 1.2. During the training process, more than 200 sets of the data obtained from the validated CFD model were adopted to train the SVM. Consequently, the optimal separation plane between two patterns was built with SVM automatically and a classification model was developed to identify the deformation of the printed filament according to the knowledge based on learning data. The predicted pattern from the training data together with corresponding deformation of the printed filament is shown in Fig. 11.

The plane representing the deformation of the printed filament is 1.2. All the data points above the plane means that the deformation of the printed filament is smaller than 1.2. On the contrary, all the data points below the plane means that the deformation of the printed filament is larger than 1.2. The accuracy of the SVM model is higher than 0.9 in this study. It is clear from Fig. 11 that the slope of the plane along the plastic viscosity axis is nearly zero, especially when the yield stress is larger, which means that the effect of the material plastic viscosity on the deformation of the printed filament could be minor at high yield stress conditions when changing the nozzle travel speed during the printing process. A similar phenomenon was observed when the nozzle travel speed was equal to the material inlet velocity. However, the impact of material yield stress on the deformation of the printed filament is quite different. When material yield stress is higher than approximately 450 Pa, the nozzle travel speed decrease progressively to keep the deformation of the printed filament constant, this shows that the nozzle travel speed can affect the deformation of the printed filament significantly. According to the conservation of volume, the relationship between nozzle cross-section area and fluid velocity can be described as,

$$A_1 v_i = A_2 v_n \tag{12}$$

where A_1 and A_2 (m^2) refer to the cross-section area of the nozzle and the printed filament respectively. $v_i$and v_n (m/s) represent the material inlet velocity and nozzle travel speed respectively. Rewrite Eq. (12)

$$A_2 = \frac{A_1 v_i}{v_n} = \frac{\dot{Q}}{v_n} \tag{13}$$

$\dot{Q}$ (m^3/s) is volume flow rate, which is a constant in this study. Apparently, there is an inverse proportional relationship between nozzle travel

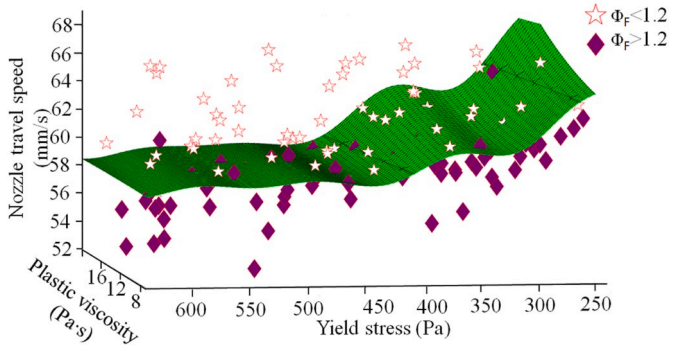

Fig. 11. SVM classification of the CFD simulated filament deformation vs material rheological properties and process parameter.

speed and the cross-section area of the printed filament. When the nozzle travel speed increases, the cross-section area of the printed filament will decrease accordingly, leading to a reduction in the deformation of the printed filament.

To investigate the deformation of the printed filament qualitatively at various nozzle travel speeds, the flow patterns and velocity distribution of the material (yield stress 516 Pa) within half of the deposit zone were studied numerically, as shown in Fig. 12. When the nozzle travels at a speed of 60 mm/s, the material flows perpendicularly at the upper part of the deposition zone (marked out with circle). In comparison, when nozzle travels at the speed of 55 mm/s, the material near the inner surface of the nozzle flows to the lower left corner (marked out with circle) after being extruded from the nozzle, causing more material deposition at the lower left corner and larger deformation of the printed filament. Apart from that, material velocity at the upper part of the deposition zone (marked out with rectangle) is high, which contributes to the increase of the local pressure at bottom zone, pressing the material to the surface of the filament as shown in Fig. 7 and widen the bottom zone of the printed filament. A similar phenomenon was observed when the nozzle ravels at an even lower speed, such as 50 mm/s. In other words, the lower nozzle travel speed, the larger deformation of the printed filament.

However, when the material yield stress is lower than 250 Pa, the nozzle travel speed increases sharply to keep the deformation of the printed filament constant, which indicates that material yield stress affects the deformation of the printed filament significantly. Overall, to keep the deformation of the printed filament constant, the nozzle travel speed should increase with the decrease of material yield stress. In other words, there is a dilemma in that high efficiency requires nozzle travel speed to be enhanced while good buildability requires high yield stress. Hence, these two key requirements are underpinned by the knowledge of correlation between nozzle travel speed and yield stress.

4.3. *Characterizing the deformation of the printed filament with the combined effect of process parameters and material rheological properties*

As mentioned above, the effect of cementitious material plastic viscosity on the deformation of the printed filament is minimal even when changing the nozzle travel speed during the printing process. Apart from that, the larger difference between the material inlet velocity and the nozzle travel speed, the larger deformation of the filament. To characterize the effect of velocity difference on the deformation of the printed filament, the relative nozzle travel speed, which refers to the ratio of nozzle travel speed to material average inlet velocity, was proposed. Then the deformation of the printed filament can be plotted on a contour diagram with two axes representing the relative nozzle travel speed and material yield stress, respectively, as shown in Fig. 13.

It is clear from Fig. 13 that when the yield stress is higher than 600 Pa, the contour line is approximately parallel to the horizontal axis (referring material yield stress). This indicates that material yield stress has little influence on the deformation of the printed filament. In other words, the yield stress is high enough to resist the flow of the cementitious material after deposition. However, when material yield stress is lower than 600 Pa, the combined effect of the velocity ratio and the yield stress affects the deformation of the printed filament greatly. Overall, it seems that the relative nozzle travel speed is more significant than the yield stress in increasing the deformation of the printed filament due to the intensive contours at the left bevel.

In order to aid the visual presentation of the deformation of the printed filament, a 3D surface figure was plotted as shown in Fig. 14. From Fig. 14, the deformation of the printed filament rises greatly as the material yield stress approaches 200 Pa and the relative nozzle travel speed is approximately 0.85, respectively. Lastly, to control the 3DCMP process, an empirical parametric associative model was proposed based on the data with high accuracy ($R^2 = 0.85$):

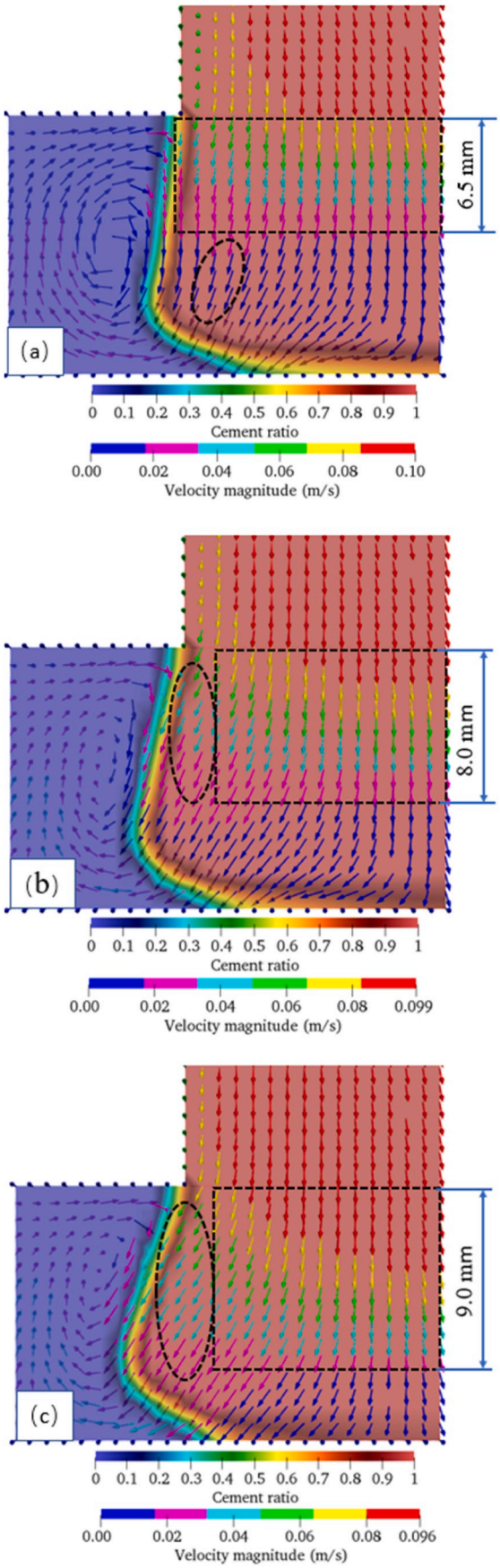

Fig. 12. The flow pattern and velocity distribution of material with various nozzle travel speeds V_n (a) $V_n = 60$ mm/s, (b) $V_n = 55$ mm/s, (c) $V_n = 50$ mm/s.

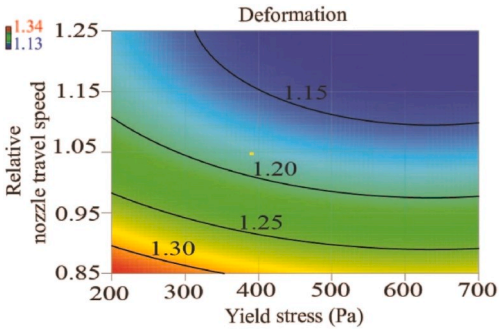

Fig. 13. Contour for deformation of the printed filament.

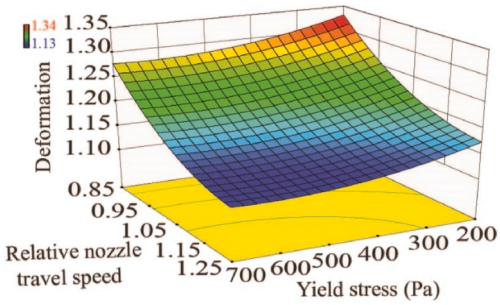

Fig. 14. 3D surface diagram for the deformation of the printed filament.

$$\Phi_F = 2.6 - 3.6{\cdot}A - 2.12{\cdot}B + 2.83 \times 10^{-7}A^2 + 0.82A^2 \quad (14)$$

Where Φ_F, A and B represent the deformation of the printed filament, material yield stress and relative nozzle travel speed, respectively.

5. Conclusions

The purposes of this study are to investigate of the flow behaviour of the cementitious material during the extrusion and deposit process and develop a SVM model to study the effects of material rheological properties and process parameters and their combinations on the deformation of the printed filament. The SVM model is based on the machine learning approach for the pattern classification of the deformation of the printing filament in 3DCMP with training data from the experimental validated numerical model. Based on the modelling above, the following main conclusions can be derived:

1) A numerical model has been proposed to study the flow mechanism of the cementitious material during the extrusion and deposition process. Experiments have been conducted to validate the accuracy of the numerical model.
2) The SVM model based on machine learning was implemented successfully to classify the pattern of the deformation of the printed filament in relation to various material rheological properties and process parameters.
3) The 2D and 3D predicted patterns from SVM model show that the impact of material plastic viscosity on the deformation of the printed filament is minor, while the relative nozzle travel speed and material yield stress significantly affects the deformation of the printed filament.
4) An empirical model was proposed to characterize the deformation of the printed filament and the relative nozzle travel speed and material yield stress.

With regard to future work, although the machine learning based SVM model performs well in pattern classification, how classification can be used to develop the data driven in line monitoring and create diagnosis system of the 3D cementitious material printing process is still on going.

Declaration of competing interest

The authors declare no conflict of interest.

CRediT authorship contribution statement

Zhixin Liu: Methodology, Investigation, Writing - original draft. **Mingyang Li:** Conceptualization, Methodology, Writing - original draft, Writing - review & editing. **Yiwei Weng:** Writing - original draft, Writing - review & editing. **Ye Qian:** Writing - original draft, Writing - review & editing. **Teck Neng Wong:** Conceptualization, Methodology, Writing - review & editing. **Ming Jen Tan:** Validation, Writing - review & editing.

Acknowledgment

This research is supported by the National Research Foundation, Prime Minister's Office, Singapore under its Medium-Sized Centre funding scheme, Sembcorp Design & Construction Pte Ltd, and Sembcorp Architects & Engineers Pte Ltd.

Appendix B. Supplementary data

Supplementary data to this article can be found online at https://doi.org/10.1016/j.compositesb.2020.108018.

Appendix A

No.	Plastic viscosity k (Pa·s)	Dynamic yield stress τ_0(Pa)	Nozzle travel speed Vn (m/s)	Simulated Deformation Φ_F
1	14.624	448.676	0.060	1.197
2	15.872	258.199	0.060	1.219
3	6.247	332.066	0.060	1.211
4	16.150	269.247	0.060	1.215
5	10.555	276.572	0.060	1.218
6	5.520	491.541	0.060	1.192
7	8.226	435.737	0.060	1.196
8	10.431	341.265	0.060	1.211
9	19.371	264.412	0.060	1.215
10	7.080	369.928	0.060	1.204
11	19.873	355.783	0.060	1.213

(*continued on next page*)

(*continued*)

No.	Plastic viscosity k (Pa·s)	Dynamic yield stress τ_0(Pa)	Nozzle travel speed Vn (m/s)	Simulated Deformation Φ_F
12	17.593	472.636	0.060	1.193
13	9.878	479.419	0.060	1.194
14	14.035	309.231	0.060	1.213
15	6.825	383.449	0.060	1.204
16	9.402	377.721	0.060	1.205
17	16.874	408.998	0.060	1.198
18	13.692	452.027	0.060	1.198
19	18.763	460.183	0.060	1.193
20	11.824	324.095	0.060	1.212
21	5.085	431.274	0.060	1.197
22	15.207	421.349	0.060	1.197
23	17.225	294.084	0.060	1.217
24	12.041	292.013	0.060	1.215
25	13.357	390.176	0.060	1.201
26	12.621	505.334	0.060	1.193
27	8.623	345.367	0.060	1.211
28	11.310	405.322	0.060	1.200
29	7.716	315.497	0.060	1.213
30	8.370	570.030	0.060	1.189
31	7.620	676.170	0.060	1.183
32	17.740	646.530	0.060	1.184
33	18.950	543.370	0.060	1.185
34	5.160	511.340	0.060	1.192
35	11.060	617.350	0.060	1.184
36	13.790	600.230	0.060	1.187
37	16.610	558.000	0.060	1.185
38	8.608	200.334	0.060	1.226
39	15.100	116.150	0.060	1.312
40	17.590	213.550	0.060	1.235
41	12.930	142.220	0.060	1.245
42	19.670	101.430	0.060	1.380
43	7.820	235.300	0.060	1.220
44	10.550	228.420	0.060	1.224
45	6.020	158.330	0.060	1.245
46	18.000	625.000	0.060	1.186
47	5.000	200.000	0.060	1.229
48	5.500	100.000	0.060	1.325
49	21.000	550.000	0.060	1.186

References

[1] C.K. Chua, K.F. Leong, 3D printing and additive manufacturing: Principles and applications (with Companion Media Pack) of Rapid Prototyping fourth ed., World Scientific Publishing Company2014.

[2] Paul SC, van Zijl GP, Tan MJ, Gibson I. A review of 3D concrete printing systems and materials properties: current status and future research prospects. Rapid Prototyp J 2018;24(4):784–98.

[3] Liu Z, Li M, Wong TN, Tan MJ. Measurement of the fresh rheological properties of material in 3D printing. 2018.

[4] Weng Y, Li M, Liu Z, Lao W, Lu B, Zhang D, Tan MJ. Printability and fire performance of a developed 3D printable fibre reinforced cementitious composites under elevated temperatures. Virtual Phys Prototyp 2019;14(3):284–92.

[5] Panda B, Ruan S, Unluer C, Tan MJ. Improving the 3D printability of high volume fly ash mixtures via the use of nano attapulgite clay. Compos B Eng 2019;165:75–83.

[6] Asprone D, Auricchio F, Menna C, Mercuri V. 3D printing of reinforced concrete elements: technology and design approach. Construct Build Mater 2018;165:218–31.

[7] Ma G, Li Z, Wang L, Wang F, Sanjayan J. Mechanical anisotropy of aligned fiber reinforced composite for extrusion-based 3D printing. Construct Build Mater 2019;202:770–83.

[8] Le TT, Austin SA, Lim S, Buswell RA, Gibb AG, Thorpe T. Mix design and fresh properties for high-performance printing concrete. Mater Struct 2012;45(8):1221–32.

[9] Nerella VN, Mechtcherine V. Studying the Printability of fresh concrete for formwork-Free concrete Onsite 3D printing Technology (CONPrint3D), 3D concrete printing Technology. Elsevier; 2019. p. 333–47.

[10] Asprone D, Menna C, Bos FP, Salet TA, Mata-Falcón J, Kaufmann W. Rethinking reinforcement for digital fabrication with concrete. Cement Concr Res 2018;112:111–21.

[11] Tay YWD, Qian Y, Tan MJ. Printability region for 3D concrete printing using slump and slump flow test. Compos B Eng 2019;174:106968.

[12] Li Z, Li W, Ma G. Mechanical improvement of continuous steel microcable reinforced geopolymer composites for 3D printing subjected to different loading conditions. Compos B Eng 2020:107796.

[13] Nguyen K, Navaratnam S, Mendis P, Zhang K, Barnett J, Wang H. Fire safety of composites in prefabricated buildings: from fibre reinforced polymer to textile reinforced concrete. Compos B Eng 2020:107815.

[14] Bastani AF, Aukrust T, Brandal S. Optimisation of flow balance and isothermal extrusion of aluminium using finite-element simulations. J Mater Process Technol 2011;211(4):650–67.

[15] Kwon H, Bukkapatnam S, Khoshnevis B, Saito J. Effects of orifice shape in contour crafting of ceramic materials. Rapid Prototyp J 2002;8(3):147–60.

[16] Lao W, Li M, Masia L, Tan MJ. Approaching rectangular extrudate in 3D printing for building and construction by experimental Iteration of nozzle design. 2017.

[17] Panda B, Lim JH, Tan MJ. Mechanical properties and deformation behaviour of early age concrete in the context of digital construction. Compos B Eng 2019;165:563–71.

[18] Serdeczny MP, Comminal R, Pedersen DB, Spangenberg J. Experimental validation of a numerical model for the strand shape in material extrusion additive manufacturing. Additive Manufact. 2018;24:145–53.

[19] Comminal R, Serdeczny MP, Pedersen DB, Spangenberg J. Numerical modeling of the strand deposition flow in extrusion-based additive manufacturing. Additive Manufact. 2018;20:68–76.

[20] Bellini A. Fused deposition of ceramics: a comprehensive experimental, analytical and computational study of material behavior, fabrication process and equipment design. 2002.

[21] Comminal RB, Hattel JH, Spangenberg J. Numerical simulations of planar extrusion and fused filament fabrication of non-Newtonian fluids. Nordic Rheology Soc. Ann. Trans. 2017;25:263–70.

[22] Xia H, Lu J, Dabiri S, Tryggvason G. Fully resolved numerical simulations of fused deposition modeling. Part I: fluid flow. Rapid Prototyp J 2018;24(2):463–76.

[23] Du J, Wei Z, Wang X, Wang J, Chen Z. An improved fused deposition modeling process for forming large-size thin-walled parts. J Mater Process Technol 2016;234:332–41.

[24] McIlroy C, Olmsted PD. Deformation of an amorphous polymer during the fused-filament-fabrication method for additive manufacturing. J Rheol 2017;61(2):379–97.

[25] Liu J, Anderson KL, Sridhar N. Direct simulation of polymer fused deposition modeling (FDM)-An implementation of the multi-phase viscoelastic solver in OpenFOAM. Int J Comput Methods 2018:1844002.

[26] Kwon H. Experimentation and analysis of contour crafting (CC) process using uncured ceramic materials. University of Southern California Los Angeles; 2002.

[27] Bos F, Wolfs R, Ahmed Z, Salet T. Additive manufacturing of concrete in construction: potentials and challenges of 3D concrete printing. Virtual Phys Prototyp 2016;11(3):209–25.
[28] Chanda T, Zhou J, Duszczyk J. A comparative study on iso-speed extrusion and isothermal extrusion of 6061 Al alloy using 3D FEM simulation. J Mater Process Technol 2001;114(2):145–53.
[29] Kruger J, Cho S, Zeranka S, Viljoen C, van Zijl G. 3D concrete printer parameter optimisation for high rate digital construction avoiding plastic collapse. Compos B Eng 2020;183:107660.
[30] Tay YWD, Li MY, Tan MJ. Effect of printing parameters in 3D concrete printing: printing region and support structures. J Mater Process Technol 2019;271:261–70.
[31] Abdul-Jawwad AK, Bashir A. A comprehensive model for predicting profile exit temperature of industrially extruded 6063 aluminum alloy. Mater Manuf Process 2011;26(2):193–201.
[32] Li N, Shi C, Zhang Z, Wang H, Liu Y. A review on mixture design methods for geopolymer concrete. Compos B Eng 2019:107490.
[33] Chen L, Liu Z, Sun P, Huo W. Formulation of a fuel spray SMD model at atmospheric pressure using Design of Experiments (DoE). Fuel 2015;153:355–60.
[34] Yao Z, Mei D, Chen Z. On-line chatter detection and identification based on wavelet and support vector machine. J Mater Process Technol 2010;210(5):713–9.
[35] Kothuru A, Nooka SP, Liu R. Application of audible sound signals for tool wear monitoring using machine learning techniques in end milling. Int J Adv Manuf Technol 2018;95(9–12):3797–808.
[36] Cho S, Asfour S, Onar A, Kaundinya N. Tool breakage detection using support vector machine learning in a milling process. Int J Mach Tool Manufact 2005;45 (3):241–9.
[37] Chiu N-H, Guao Y-Y. State classification of CBN grinding with support vector machine. J Mater Process Technol 2008;201(1–3):601–5.
[38] Rao KV, Murthy P. Modeling and optimization of tool vibration and surface roughness in boring of steel using RSM, ANN and SVM. J Intell Manuf 2018;29(7): 1533–43.
[39] Hsueh Y-W, Yang C-Y. Tool breakage diagnosis in face milling by support vector machine. J Mater Process Technol 2009;209(1):145–52.
[40] Zhou X, Jiang P, Wang X. Recognition of control chart patterns using fuzzy SVM with a hybrid kernel function. J Intell Manuf 2018;29(1):51–67.
[41] Roussel N. Rheological requirements for printable concretes. Cement Concr Res 2018;112:76–85.
[42] Lachemi M, Hossain K, Lambros V, Nkinamubanzi P-C, Bouzoubaa N. Performance of new viscosity modifying admixtures in enhancing the rheological properties of cement paste. Cement Concr Res 2004;34(2):185–93.
[43] Zhang H, Moon SK, Ngo TH. A hybrid machine learning method to determine optimal operating process window in aerosol jet 3D printing. ACS Appl Mater Interfaces 2019;11:17994–8003.
[44] Grandes FA, Sakano VK, Rego AC, Cardoso FA, Pileggi RG. Squeeze flow coupled with dynamic pressure mapping for the rheological evaluation of cement-based mortars. Cement Concr Compos 2018;92:18–35.
[45] Wallevik JE. Rheology of particle suspensions: fresh concrete, mortar and cement paste with various types of lignosulfonates. Fakultet for ingeniørvitenskap og teknologi; 2003.
[46] Liu Z, Li M, Weng Y, Wong TN, Tan MJ. Mixture Design Approach to optimize the rheological properties of the material used in 3D cementitious material printing. Construct Build Mater 2019;198:245–55.